5. Kodama, R. *et al.* Fast heating of ultrahigh-density plasma as a step towards laser fusion ignition. *Nature* **412**, 798–802 (2001).

6. Hoshino, M., Mukai, T., Yamamoto, T. & Kokubun, S. Ion dynamics in magnetic reconnection: Comparison between numerical simulation and Geotail observations. *J. Geophys. Res.* **103**, 4509–4530 (1998).

7. Baumjohann, W., Paschmann, G. & Cattell, C. A. Average plasma properties in the central plasma sheet. *J. Geophys. Res.* **94**, 6597–6606 (1989).

8. Gary, S. P. Electromagnetic ion/ion instabilities and their consequences in space plasmas—A review. *Space Sci. Rev.* **56**, 373–415 (1991).

9. Delcourt, D. C., Moore, T. E. & Chappell, C. R. Contribution of low-energy ionospheric protons to the plasma sheet. *J. Geophys. Res.* **99**, 5681–5689 (1994).

10. Arzner, K. & Scholer, M. Kinetic structure of the post plasmoid plasma sheet during magnetotail reconnection. *J. Geophys. Res.* **106**, 3827–3844 (2001).

11. Lakhina, G. S., Tsurutani, B. T., Kojima, H. & Matsumoto, H. "Broadband" plasma waves in the boundary layers. *J. Geophys. Res.* **105**, 27791–27831 (2000).

12. Saito, Y. *et al.* Slow-mode shocks in the magnetotail. *J. Geophys. Res.* **100**, 23567–23581 (1995).

13. Hirahara, M. *et al.* Acceleration and heating of cold ion-beams in the plasma sheet boundary layer observed with GEOTAIL. *Geophys. Res. Lett.* **21**, 3003–3006 (1994).

14. Nishida, A., Mukai, T., Yamamoto, T., Kokubun, S. & Maezawa, K. A unified model of the magnetotail convection in geomagnetically quiet and active times. *J. Geophys. Res.* **103**, 4409–4418 (1998).

15. Abe, T. *et al.* Observations of polar wind and thermal ion outflow by Akebono/SMS. *J. Geomagn. Geoelectr.* **48**, 319–325 (1996).

16. Seki, K. *et al.* On atmospheric loss of oxygen ions from earth through magnetospheric processes. *Science* **291**, 1939–1941 (2001).

Relating atomic-scale electronic phenomena to wave-like quasiparticle states in superconducting Bi2Sr2CaCu2O8+δ

K. McElroy[*][†], **R. W. Simmonds**[*], **J. E. Hoffman**[*], **D.-H. Lee**[*][†][‡], **J. Orenstein**[*][†], **H. Eisaki**[§], **S. Uchida**[||] **& J. C. Davis**[*][†][¶]

* Department of Physics, University of California, and † Materials Science Division, Lawrence Berkeley National Laboratory, Berkeley, California 94720, USA

‡ Center for Advanced Study, Tsinghua University, Beijing 100084, China

§ AIST, 1-1-1 Central 2, Umezono, Tsukuba, Ibaraki, 305-8568 Japan

|| Department of Physics, University of Tokyo, Yayoi, 2-11-16 Bunkyoku, Tokyo 113-8656, Japan

¶ Department of Physics, LASSP, Cornell University, Ithaca, New York 14850, USA

The electronic structure of simple crystalline solids can be completely described in terms either of local quantum states in real space (r-space), or of wave-like states defined in momentum-space (k-space). However, in the copper-oxide superconductors, neither of these descriptions alone may be sufficient. Indeed, comparisons between r-space[1–5] and k-space[6–13] studies of Bi2Sr2CaCu2O8+δ (Bi-2212) reveal numerous unexplained phenomena and apparent contradictions. Here, to explore these issues, we report Fourier transform studies of atomic-scale spatial modulations in the Bi-2212 density of states. When analysed as arising from quasiparticle interference[14–16], the modulations yield elements of the Fermi-surface and energy gap in agreement with photoemission experiments[12,13]. The consistency of numerous sets of dispersing modulations with the quasiparticle interference model shows that no additional order parameter is required. We also explore the momentum-

space structure of the unoccupied states that are inaccessible to photoemission, and find strong similarities to the structure of the occupied states. The copper oxide quasiparticles therefore apparently exhibit particle–hole mixing similar to that of conventional superconductors. Near the energy gap maximum, the modulations become intense, commensurate with the crystal, and bounded by nanometre-scale domains[4]. Scattering of the antinodal quasiparticles is therefore strongly influenced by nanometre-scale disorder.

Among the unexplained phenomena of Bi-2212 quasiparticles are: (1) the appearance of anti-nodal quasiparticles only below T_c (ref. 17); (2) the proportionality between the quasiparticle-peak intensity and both the superfluid and hole densities[18,19]; (3) the 'kink' in the nodal-quasiparticle dispersion[20,21]; (4) the apparent contradiction between nanoscale electronic disorder[1–4] and quasiparticles well-defined in k-space[22]; and (5) the nature of the vortex-core-induced electronic states[23]. Here we focus on the possibility that some of these phenomena emerge from the special relationship between r-space and k-space that is characteristic of the strongly correlated electronic structure of the copper oxides.

To explore this relationship we use Fourier transform scanning tunnelling spectroscopy (FT-STS). In this technique, the tip-sample differential tunnelling conductance ($g = dI/dV$) is spatially mapped
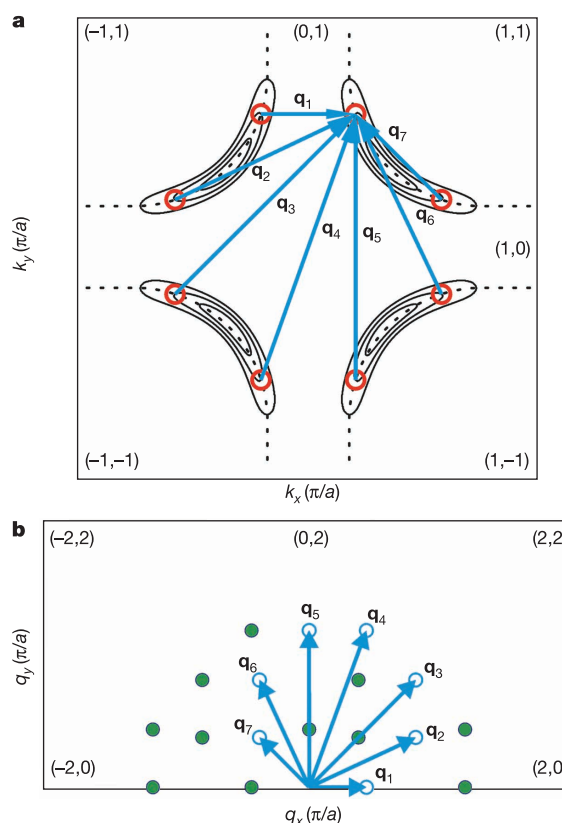

Figure 1 The expected wavevectors of quasiparticle interference patterns in a superconductor with electronic band structure like that of Bi-2212. **a**, Solid lines indicate the **k**-space locations of several banana-shaped quasiparticle CCE as they increase in size with increasing energy. As an example, at a specific energy, the octet of regions of high $|\nabla_k E(\mathbf{k})|^{-1}$ are shown as red circles. The seven primary scattering **q**-vectors interconnecting elements of the octet are shown in blue. **b**, Each individual scattering **q**-vector from this set of seven is shown as a blue arrow originating from the origin in **q**-space, and ending at a point given by a blue circle. The end points of all other inequivalent **q**-vectors of the octet model (as determined by mirroring each of the original seven in the symmetry planes of the Brillouin zone) are shown as solid green circles. Thus, if the quasiparticle interference model is correct, there would be sixteen inequivalent local maxima in the inequivalent half of **q**-space detectable by FT-STS.
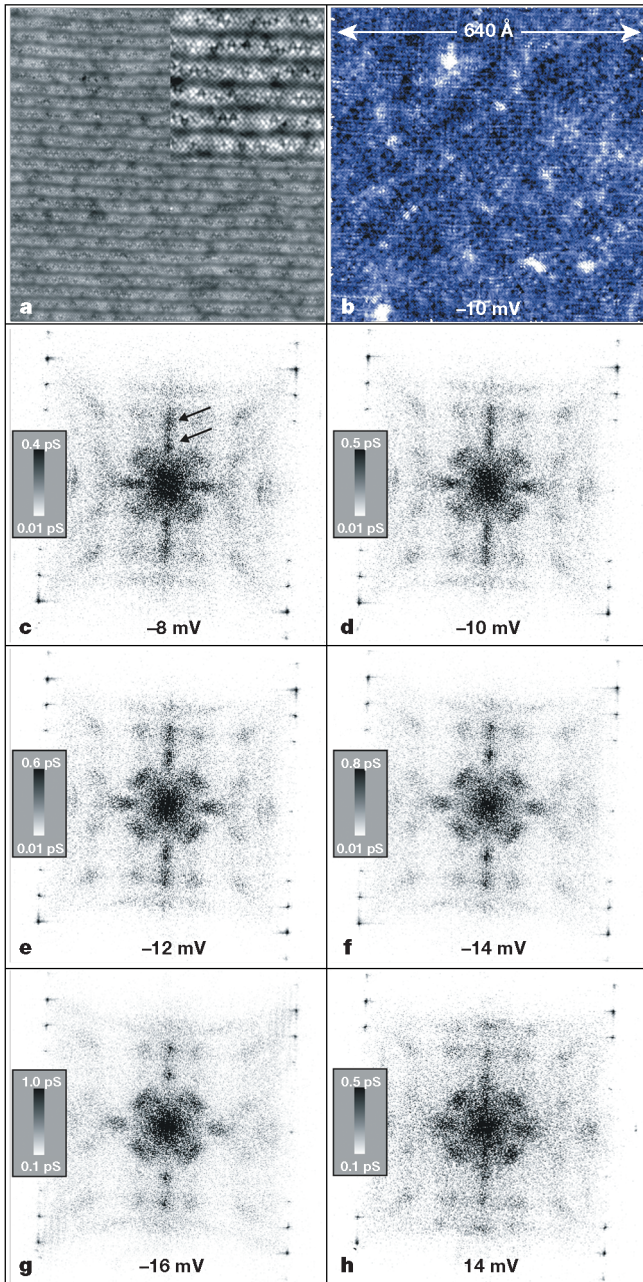
Figure 2 Atomic resolution images of the LDOS and the resulting Fourier-space images of the wavevectors making up the *LDOS* modulations. **a**, A topographic image of the BiO surface used, with location and resolution identical to the LDOS maps. The × 2 magnification inset (from part of the same image) demonstrates the quality of atomic resolution achieved. **b**, Representative example of the real space $g(\mathbf{r},\omega)$ in this field of view. All $g(\mathbf{r},\omega)$ were acquired using the same atomic resolution and register. **c**–**g**, Examples of the $g(\mathbf{q},\omega)$ at five different energies. The only non-dispersive signals (which are due to the supermodulation) are marked by arrows in **c**. The reciprocal atomic lattice is located at the square box of intense points at the side of each panel. One can readily see 12 of the 16 LDOS modulations of the quantum interference model. The dispersion and evolution of all the wavevectors of these modulations is evident in the differences between frames. Careful examination reveals that, in addition to the slowly dispersing $\mathbf{q}_1$ signal moving to $|\mathbf{q}| < \pi/2a_0$ with increasing energy, there is no additional signal above the noise at $\mathbf{q} = (1/4,0)2\pi/a_0$ or $\mathbf{q} = (0,1/4)2\pi/a_0$ (as proposed for a coexisting charge density wave (CDW) order parameter). **h**, The $g(\mathbf{q},\omega)$ measured from the empty states at +14 meV above the Fermi level. It is similar but not identical to the $g(\mathbf{q},\omega)$ at −14 meV in Fig. 2f, presumably because of the effects of normal-state band structure on the quasiparticle interference process.

at each bias voltage *V*. The result, $g(\mathbf{r},\omega)$, is proportional to the local density of states (LDOS) at location **r** and energy $\omega = eV$. In metals[24] and more recently in a copper oxide superconductor[5], quasiparticle interference has been observed. It is manifest as spatial modulations in $g(\mathbf{r},\omega)$ whose wavelengths λ (or wavevectors $q = 2\pi/\lambda$) change with energy. In FT-STS, the **q**-vectors of these modulations can be determined from the locations of peaks in $g(\mathbf{q},\omega)$, the Fourier transform magnitude of $g(\mathbf{r},\omega)$.

We focus on Bi-2212, a material whose quasiparticle dispersion $E(\mathbf{k})$ has been mapped for the filled states by ARPES[12,13], and which exhibits four nodes in $\Delta(\mathbf{k})$. A contour plot of quasiparticle energy (ω) in **k**-space helps to visualize this situation. For $|\omega| < \Delta_0$ (the maximal gap), the contours of constant quasiparticle energy (CCE) are banana-shaped, as shown in Fig. 1a. With such unusual **k**-space structures, elastic quasiparticle scattering should produce striking consequences in $g(\mathbf{r},\omega)$. The reason is that the quasiparticle density of states at ω, $n(\omega)$, is proportional to

$$\int_{E(\mathbf{k})=\omega} |\nabla_k E(\mathbf{k})|^{-1}\, dk \qquad (1)$$

Because each 'banana' exhibits its largest rate of increase with energy $|\nabla_k E(\mathbf{k})|^{-1}$ near its two ends, equation (1) shows that the primary contributions to $n(\omega)$ come from the octet of momentum-space regions centred around the end points $\mathbf{k}_j(\omega)$; $j = 1, 2, \ldots 8$. A particular octet is indicated by red circles in Fig. 1a.

During elastic scattering, a quasiparticle located near one element of the octet will very probably be scattered to the vicinity of another element, because of the large joint density of states between them. Owing to quantum interference[5], such scattering produces spatial LDOS modulations with wavevector $\mathbf{q} = \mathbf{k}_{final} - \mathbf{k}_{initial}$ and with intensity proportional to $n_{initial}(\omega)n_{final}(\omega)$ (the joint density of states). Therefore pairs of states with high $n_{initial}(\omega)n_{final}(\omega)$ should generate the most intense LDOS modulations. The wavevectors $\mathbf{q}_i(\omega)$ of these modulations would then be determined by all possible pairs of points in the octet $\mathbf{k}_j(\omega)$. By considering just one $\mathbf{k}_j$ in a representative octet (Fig. 1a) we see that, at each energy, there are seven characteristic scattering wavevectors $\mathbf{q}_i(\omega)$; $i = 1, 2, \ldots 7$. These are indicated by blue arrows in the **k**-space of Fig. 1a and in the **q**-space of Fig. 1b. The model then predicts a total of $8 \times 7 = 56$ sets of scattering wavevectors. Only 32 of these are inequivalent and therefore 16 distinct $\pm\mathbf{q}$ pairs could be detected by FT-STS. Previously, no more than four sets of wavevectors have been detected[5,25].

We use float-zone-fabricated Bi-2212 single crystals which are as-grown (slightly overdoped) with $T_c = 86$ K. They are cleaved (at the BiO plane) in cryogenic ultrahigh vacuum and immediately inserted into the scanning tunnelling microscope head at 4.2 K. A search for all sets of **q**-vectors requires that each $g(\mathbf{r},\omega)$ contain Fourier components with $|\mathbf{q}| \gtrsim 2\pi/a_0$, so atomic resolution is required in all $g(\mathbf{r},\omega)$. Even more importantly, to obtain sufficient **q**-space resolution $\Delta q = 2\pi/L$ so that the dispersions of all sets of **q**-vectors can be resolved, it is necessary that $g(\mathbf{r},\omega)$ be measured in a field of view $L > 450$ Å. Fig. 2a shows the topographic image of the 640-Å-square field of view used for all studies reported here. We emphasize that this atomic resolution and position registry were maintained for all $g(\mathbf{r},\omega)$ measurements. Figure 2b shows a typical example of a measured $g(\mathbf{r},\omega)$ in which the LDOS modulations are clearly evident. Figure 2c–g are representative $g(\mathbf{q},\omega)$ for several negative ω. No interpolation, smoothing or filtering is used on any image in this paper.

Neglecting effects of the supermodulation, all the $g(\mathbf{q},\omega)$ in Fig. 2 are clearly fourfold symmetric and display numerous local maxima (dark regions) at different **q** for different energies. Quasiparticle interference has long been predicted for the copper oxides[14]. After ref. 5, new theoretical analyses[15,16,26,27] were carried out, yielding predictions of up to 16 inequivalent peaks in $g(\mathbf{q},\omega)$. These peaks are predicted to exhibit a specific fourfold symmetric pattern and to

disperse, self-consistently, along trajectories set by the Fermi surface, and $|\Delta(\mathbf{k})|$. The unprocessed data in Fig. 2 are in good qualitative agreement with these predictions.

To analyse these data further, we use the location of the peaks we can detect in $g(\mathbf{q}, \omega)$ between $-6\,\mathrm{meV} > \omega > -30\,\mathrm{meV}$ (from the quadrant or $\mathbf{q}$-space without the supermodulation). This yields about 90 different $\mathbf{q}_i(\omega)$ whose magnitudes $|\mathbf{q}_i(\omega)|$ are plotted in
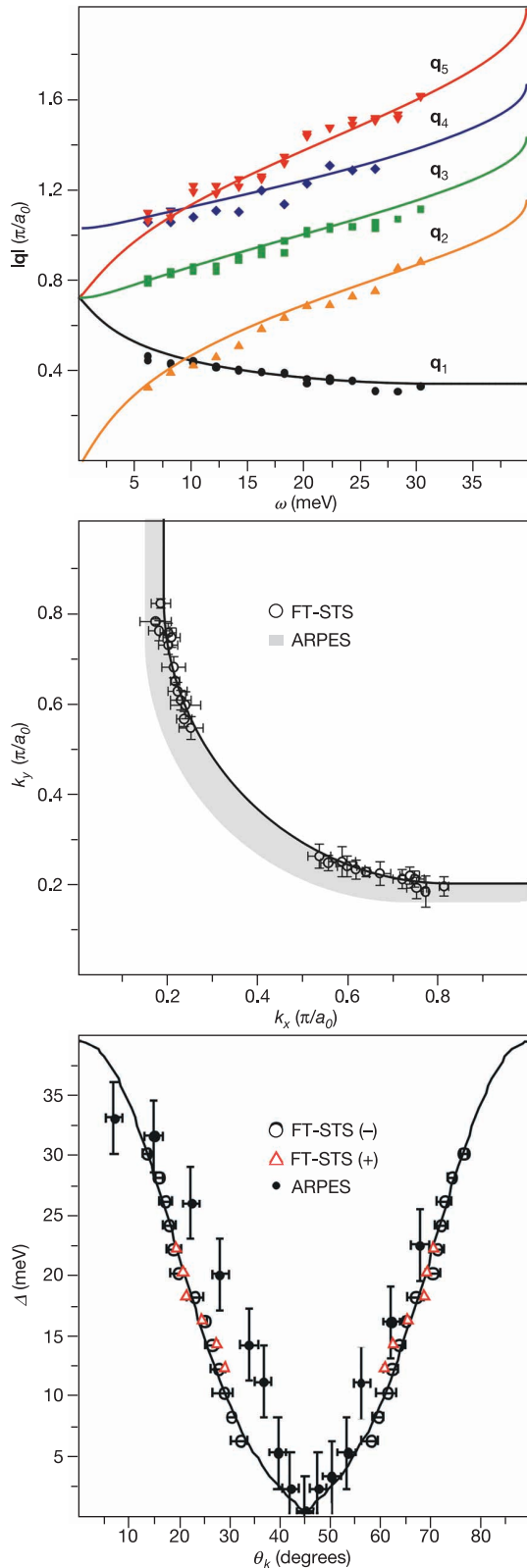
Fig. 3a. From these data, the locus from which the scattering originates $\mathbf{k}_s$ and energy-gap $\Delta(\mathbf{k})$ can be estimated by assuming that each:

$$\mathbf{q}_i(\omega) = \mathbf{k}_m(\omega) - \mathbf{k}_n(\omega) \qquad (2)$$

where $\mathbf{k}_m(\omega)$ and $\mathbf{k}_n(\omega)$ are necessarily among the octet of states $\mathbf{k}_j(\omega)$ at ω. Using the mirror symmetries of the Brillouin zone plus equation (2), the location of the octet elements, $\mathbf{k}_s(\omega)$, can be determined from the $\mathbf{q}_i(\omega)$. Our FT-STS measured $\mathbf{k}_s(\omega)$ for the filled electronic states between $-6\,\mathrm{meV} > \omega > -30\,\mathrm{meV}$ is shown as open circles in Fig. 3b. We interpret it as the k-space trajectory of the ends of the CCE 'bananas' or, in quantum interference models[14–16], the normal-state Fermi surface. Because of the large number of $\mathbf{q}_i(\omega)$ measured for each ω, we can check the internal consistency of our data within the interference model using numerous independent observations. To do so we use at least five independent combinations of $\mathbf{q}_i(\omega)$ in equation (2) to identify $\mathbf{k}_s(\omega)$ at each ω. The error bars surrounding the data points in Fig. 3b are the statistical standard deviation in each $\mathbf{k}_s(\omega)$ resulting from these different combinations. Their small sizes demonstrate how these dispersive $\mathbf{q}$-vectors are quite self-consistent within the interference model.

We can also measure the superconducting energy gap function $\Delta(\mathbf{k}_s)$ from the data in Fig. 3a. For a given $\omega = eV$, we find the associated $\mathbf{k}_s$ and plot $\omega(\mathbf{k}_s)$, the energy at which quasiparticle scattering is intense along the trajectory $\mathbf{k}_s$. Within these models[14–16], this is the momentum dependence of the superconducting energy gap $\Delta(\mathbf{k}_s)$. Following ARPES notation, $\mathbf{k}_s$ is parameterized by using the angle θ_k about (π, π). Our results for $\Delta(\theta_k)$ are shown as open circles in Fig. 3c and given by:

$$\Delta(\theta_k) = \Delta_0[A\cos(2\theta_k) + B\cos(6\theta_k)] \qquad (3)$$

With $\Delta_0 = 39.3\,\mathrm{meV}$, $A = 0.818$, $B = 0.182$ (solid line in Fig. 3c).

We now discuss the various implications of our results. First, to compare $\mathbf{k}_s(\omega)$ and $\Delta(\theta_k)$ from FT-STS with those from photoemission, we plot the Fermi surface estimated from ARPES (on a sample of similar doping[10]) as the grey band in Fig. 3b and the ARPES-derived $\Delta(\theta_k)$ as solid circles in Fig. 3c. We note the good agreement between these results from two very different spectroscopic techniques. This agreement demonstrates the link between $\mathbf{r}$-space and $\mathbf{k}$-space characteristics of the copper oxide electronic structure, it gives enhanced confidence in both techniques because the matrix elements for photoemission and tunnelling are quite different, and it demonstrates that the proposed attribution of the nanoscale

Figure 3 The measured dispersion of all sets of $\mathbf{q}$-vectors, the resulting FT-STS-derived locus of scattering, the anisotropic energy gap, and the relevant ARPES data for comparison. a, A plot of the magnitude of $\mathbf{q}_1$ through $\mathbf{q}_7$ (excluding $\mathbf{q}_4$) as a function of energy. The solid lines represent theoretical predictions based on fits to the $\mathbf{k}_s(\omega)$ and $\Delta(\mathbf{k}_s)$ as determined from FT-STS data. All the measured $\mathbf{q}$-vectors are notably consistent with each other within the model. Below $\omega = 6\,\mathrm{meV}$ LDOS modulations are difficult to detect, possibly because of strong effects of some unitary scattering resonances in the field of view or because of effects of the very low density of states near the nodal points[15]. b, The locus of scattering $\mathbf{k}_s(\omega)$ extracted using only the measured position of scattering vectors $\mathbf{q}_1$ to $\mathbf{q}_7$ (excluding $\mathbf{q}_4$). The solid line is a fit to the data, assuming the Fermi surface is the combination of a circular arc joined with two straight lines. The grey band represents measurements of the Fermi surface location made using the ARPES technique[10]. The error bars represent the statistical variations in a given $\mathbf{k}_s(\omega)$ when it is calculated using at least five different $\mathbf{q}_i(\omega)$. c, A plot of the energy gap $\Delta(\theta_k)$ determined from the filled-state measurements, shown as open circles. These were extracted using the measured position of scattering vectors $\mathbf{q}_1$ through $\mathbf{q}_7$ (excluding $\mathbf{q}_4$) in Fig. 3a. The solid line is a fit to the data. The open squares represent $\Delta(\theta_k)$ determined using ARPES techniques[10]. The red, open triangles are the $\Delta(\theta_k)$ as determined from the unoccupied state measurements at positive bias as described in the text. They are in very good agreement with those from the filled states. The mean value of Δ_0 for this near-optimal sample was 39 meV.

electronic disorder detected by STS[1–4] to surface damage not present in ARPES studies cannot be correct.

Second, the high-precision $g(\mathbf{q},\omega)$ data presented here are relevant to proposals that LDOS modulations in Bi-2212 might result from the existence of a second charge-density wave order parameter with fixed $\mathbf{q}$-vector, for example, stripes[25]. In such models $g(\mathbf{q},\omega)$ should exhibit only two non-dispersive peaks (or four non-dispersive peaks for twinned stripe domains). By contrast, quantum interference models predict 16 sets of dispersive $\mathbf{q}$-vectors consistent with each other, the Fermi-surface, and $\Delta(\mathbf{k}_s)$. Clearly this is far more consistent with our data. More recent proposals[26–29] suggest that a set of non-dispersive LDOS modulations due to fluctuations of a charge- or spin-ordered state might coexist with the quasiparticle interference patterns. We do not observe such a non-dispersive signal in addition to the quasiparticle interference effects, in the $g(\mathbf{q},\omega)$ of these as-grown samples (except for crystalline effects). In principle, however, one cannot rule out the possibility of such a hypothetical non-dispersive signal because its intensity could be arbitrarily weak. Overall, our data demonstrate that quasiparticle interference is by far the predominant effect.

Third, we discuss the quantum mechanical description of the copper oxide quasiparticles. Bogoliubov quasiparticles are the excited states of a conventional Bardeen–Cooper–Schrieffer (BCS) superconductor: quantum-coherent mixtures of particles and holes. It is important to determine whether the copper oxide quasiparticles are of this type. A strong experimental indication consistent with Bogoliubov quasiparticles is the presence of two identical branches of quasiparticle dispersion $\pm E(\mathbf{k})$. Although efforts have been made to study the positive branch $+E(\mathbf{k})$ by

photoemission[30], it has proved challenging because the Fermi function terminates photoemission intensity from these unoccupied states. By using FT-STS we can probe the momentum-space structure of the positive branch by measuring $g(\mathbf{q},\omega)$ at positive sample bias (tunnelling into unoccupied states). If identical positive and negative branches $\pm E(\mathbf{k})$ exist, the LDOS modulations at positive bias should be consistent with the negative-bias $\Delta(\mathbf{k})$ in Fig. 3. A representative example of positive bias $g(\mathbf{q},\omega)$ measured at $\omega = +14\,\mathrm{meV}$ is shown in Fig. 2h. Comparison with that at $\omega = -14\,\mathrm{meV}$ shows them to be similar but not identical, as are all measured pairs $g(\mathbf{q}, \pm \omega)$. However, when the positive branch interference wavevectors $\mathbf{q}_i(+\omega)$ are measured, the deduced $\Delta(\mathbf{k})$ (triangles in Fig. 3c) is indistinguishable within errors from that of the filled-state $\Delta(\mathbf{k})$ (open circles in Fig. 3c). This provides evidence that, in momentum-space, the copper oxide quasiparticles are particle–hole superpositions, consistent with the Bogoliubov description.

Fourth, the data can also be used to explore implications of the nanoscale electronic disorder in Bi-2212 (refs 1–4). Figure 2 shows that at $|q| < 0.15$ there is a strong response in $g(\mathbf{q},\omega)$ for all ω. These are apparent as dark regions near the centre of each panel in Fig. 2c–h. This may reflect long-wavelength inhomogeneity in the integrated LDOS[1] and, if so, reveals an obvious candidate for weak but ubiquitous potential scattering that could produce the LDOS-modulations. We also note that the theoretical models, to date, are based on isolated point-like scatterers[14,15,16] but the real scatterers are likely to be more complex in form. In that case, the character and strength of the scatterers could cause deviations of $\mathbf{k}_s(\omega)$ (as determined here) from the real Fermi surface, whereas their spatial distribution could result in breaking the symmetry of $g(\mathbf{q},\omega)$ under 90° rotations. New microscopic models and further experiments will be required to fully explore such effects.

A final new FT-STS observation relates to the antinodal quasiparticles which are at the heart of high-T_c superconductivity. Measurements of $g(\mathbf{r},\omega)$ reveal intense LDOS modulations with wavevectors equal to the reciprocal lattice vectors $\mathbf{G}$ when $\omega \approx \Delta_0$ or equivalently when $\mathbf{k} \approx (\pi/a_0, 0)$. In a crystal, the electronic wavefunctions are a linear combination of states with wavevectors $\mathbf{k}$ and $\mathbf{k} + \mathbf{G}$ near the zone boundary. This mixing is due to Umklapp scattering off the crystal lattice and can produce intense LDOS modulations at $\mathbf{G}$ when $\mathbf{k} \approx (\pi/a_0, 0)$. However, as shown in Fig. 4, we unexpectedly find that for a given ω the Umklapp LDOS modulation signal is localized to the nanoscale regions where ω is equal to the local gap value. This implies strong nanoscale spatial variations in the quasiparticle dispersions near $\mathbf{k} = (\pi/a_0, 0)$ and therefore significant scattering. Thus, whatever the source of nanoscale electronic disorder, it appears to strongly influence the lifetimes of antinodal quasiparticles in Bi-2212. □

1. Pan, S. H. *et al.* Microscopic electronic inhomogeneity in the high-T_c superconductor Bi$_2$Sr$_2$CaCu$_2$O$_{8+x}$. *Nature* **413**, 282–285 (2001).
2. Cren, T., Roditchev, D., Sacks, W. & Klein, J. Nanometer scale mapping of the density of states in an inhomogeneous superconductor. *Euro. Phys. Lett.* **54**, 84–90 (2001).
3. Howald, C., Fournier, P. & Kapitulnik, A. Inherent inhomogeneities in the tunneling spectra of Bi$_2$Sr$_2$CaCu$_2$O$_{8-x}$ crystals in the superconducting state. *Phys. Rev. B* **64**, 100504 (2001).
4. Lang, K. M. *et al.* Imaging the granular structure of high-T_c superconductivity in underdoped Bi$_2$Sr$_2$CaCu$_2$O$_{8+\delta}$. *Nature* **415**, 412–416 (2002).
5. Hoffman, J. E. *et al.* Imaging quasiparticle interference in Bi$_2$Sr$_2$CaCu$_2$O$_8$. *Science* **297**, 1148–1151 (2002).
6. Campuzano, J. C. *et al.* Fermi surfaces of YBa$_2$Cu$_3$O$_{6.9}$ as seen by angle-resolved photoemission. *Phys. Rev. Lett.* **64**, 2308–2311 (1990).
7. Dessau, D. S. *et al.* Key features in the measured band structure of Bi$_2$Sr$_2$CaCu$_2$O$_{8+x}$: Flat bands at E_F and Fermi surface nesting. *Phys. Rev. Lett.* **71**, 2781–2784 (1993).
8. Aebi, P. *et al.* Complete Fermi surface mapping of Bi$_2$Sr$_2$CaCu$_2$O$_{8+x}$(001): Coexistence of short range antiferromagnetic correlations and metallicity in the same phase. *Phys. Rev. Lett.* **72**, 2757–2760 (1994).
9. Shen, Z.-X. *et al.* Anomalously large gap in the a-b plane of Bi$_2$Sr$_2$CaCu$_2$O$_{8+\delta}$. *Phys. Rev. Lett.* **70**, 1553–1556 (1993).
10. Ding, H. *et al.* Angle-resolved photoemission spectroscopy study of the superconducting gap anisotropy in Bi$_2$Sr$_2$CaCu$_2$O$_{8+x}$. *Phys. Rev. B.* **54**, R9678–R9681 (1996).
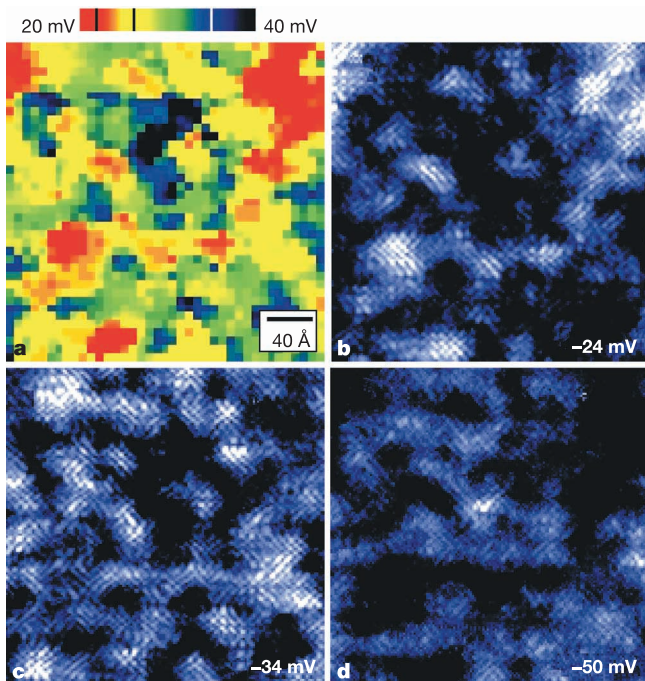
Figure 4 The electronic density of states modulations associated with antinodal quasiparticles at energies near the gap maximum. **a**, A map of the energy-gap magnitude[4] in a particular area of the surface studied in this paper (see colour scale). **b–d**, $g(\mathbf{r},\omega)$ measured at three energies, $-24\,\mathrm{meV}$, $-34\,\mathrm{meV}$ and $-50\,\mathrm{meV}$ respectively, in this exact field of view. One can immediately see, by comparison of Fig. 4a with the others, that wherever ω equals the local value of Δ, an intense 'tweed'-like pattern exists $g(\mathbf{r},\omega)$. The wavevectors of this pattern are the same in all three panels, either $\mathbf{q} = (2\pi/a_0, 0)$ or $\mathbf{q} = (0, 2\pi/a_0)$. Thus, LDOS modulations consistent with Umklapp scattering occur at different energies in adjacent nanoscale regions, signifying strong scattering of the antinodal quasiparticles.

11. Shen, Z.-X., Spicer, W. E., King, D. M., Dessau, D. S. & Wells, B. O. Photoemission studies of high-T_c superconductors: The superconducting gap. *Science* **267**, 343–350 (1995).

12. Damascelli, A., Shen, Z.-X. & Hussain, Z. Angle-resolved photoemission spectroscopy of the cuprate superconductors. Preprint at ⟨arXiV.org/cond-mat/0208504⟩ (2002).

13. Campuzano, J. C., Norman, M. R. & Randeria, M. Photoemission in the high T_c superconductors. Preprint at ⟨arXiV.org/cond-mat/0209476⟩ (2002).

14. Byers, J. M., Flatté, M. E. & Scalapino, D. J. Influence of gap extrema on tunneling conductance near an impurity in an anisotropic superconductor. *Phys. Rev. Lett.* **71**, 3363 (1993).

15. Wang, Q. & Lee, D.-H. Quasiparticle scattering interference in high temperature superconductors. *Phys. Rev. B* **67**, 020511 (2003).

16. Zhang, D. & Ting, C. S. Energy-dependent LDOS modulation in cuprate superconductors. *Phys. Rev. B* **67**, 020511 (2003).

17. Fedorov, A. V. *et al.* Temperature dependent photoemission studies of optimally doped $Bi_2Sr_2CaCu_2O_{8+\delta}$. *Phys. Rev. Lett.* **82**, 2179–2183 (1999).

18. Feng, D. L. *et al.* Signature of superfluid density in the single-particle excitation spectrum of $Bi_2Sr_2CaCu_2O_{8+\delta}$. *Science* **289**, 277–281 (2000).

19. Ding, H. *et al.* Coherent quasiparticle weight and its connection to high-T_c superconductivity from angle-resolved photoemission. *Phys. Rev. Lett.* **87**, 227001 (2001).

20. Johnson, P. D. *et al.* Doping and temperature dependence of the mass enhancement observed in the cuprate $Bi_2Sr_2CaCu_2O_{8+\delta}$. *Phys. Rev. Lett.* **87**, 177007 (2001).

21. Lanzara, A. *et al.* Evidence for ubiquitous strong electron-phonon coupling in high-temperature superconductors. *Nature* **412**, 510–514 (2001).

22. Valla, T. *et al.* Evidence for quantum critical behavior in the optimally doped cuprate $Bi_2Sr_2CaCu_2O_{8+\delta}$. *Science* **285**, 2110–2113 (1999).

23. Hoffman, J. E. *et al.* A four unit cell periodic pattern of quasiparticle states surrounding vortex cores in $Bi_2Sr_2CaCu_2O_{8+\delta}$. *Science* **295**, 466–469 (2002).

24. Crommie, M. F., Lutz, C. P. & Eigler, D. M. Imaging standing waves in a two-dimensional electron gas. *Nature* **363**, 524 (1993).

25. Howald, C., Eisaki, H., Kaneko, N. & Kapitulnik, A. Coexistence of charged stripes and superconductivity in Bi2Sr2CaCu2O8 + d. Preprint at ⟨arXiV.org/cond-mat/0201546⟩ (2002).

26. Polkovnikov, A., Sachdev, S. & Vojta, M. Spin collective mode and quasiparticle contributions to STM spectra of d-wave superconductors with pinning. Preprint at ⟨arXiV.org/cond-mat/0208334⟩ (2002).

27. Podolsky, D. *et al.* Translational symmetry breaking in the superconducting state of the cuprates: Analysis of the quasiparticle density of states. Preprint at ⟨arXiV.org/cond-mat/0204011⟩ (2002).

28. Howald, C. *et al.* Periodic density of states modulations in superconducting $Bi_2Sr_2CaCu_2O_{8+\delta}$. *Phys. Rev. B* **67**, 014533 (2003).

29. Kivelson, S. A. *et al.* How to detect fluctuating order in the high-temperature superconductors. Preprint at ⟨arXiV.org/cond-mat/0210683⟩ (2002).

30. Campuzano, J. C. *et al.* Direct observation of particle-hole mixing in the superconducting state by angle-resolved photoemission. *Phys. Rev. B* **53**, R14737–R14740 (1996).

··

A subfemtotesla multichannel atomic magnetometer

I. K. Kominis*†, T. W. Kornack*, J. C. Allred‡ & M. V. Romalis*

* *Department of Physics, Princeton University, Princeton, New Jersey 08544, USA*
‡ *Department of Physics, University of Washington, Seattle, Washington 98195, USA*

···

The magnetic field is one of the most fundamental and ubiquitous physical observables, carrying information about all electromagnetic phenomena. For the past 30 years, superconducting quantum interference devices (SQUIDs) operating at 4 K have been unchallenged as ultrahigh-sensitivity magnetic field detectors[1], with a sensitivity reaching down to $1\,\text{fT}\,\text{Hz}^{-1/2}$ ($1\,\text{fT} = 10^{-15}\,\text{T}$). They have enabled, for example, mapping of

the magnetic fields produced by the brain, and localization of the underlying electrical activity (magnetoencephalography). Atomic magnetometers, based on detection of Larmor spin precession of optically pumped atoms, have approached similar levels of sensitivity using large measurement volumes[2,3], but have much lower sensitivity in the more compact designs required for magnetic imaging applications[4]. Higher sensitivity and spatial resolution combined with non-cryogenic operation of atomic magnetometers would enable new applications, including the possibility of mapping non-invasively the cortical modules in the brain. Here we describe a new spin-exchange relaxation-free (SERF) atomic magnetometer, and demonstrate magnetic field sensitivity of $0.54\,\text{fT}\,\text{Hz}^{-1/2}$ with a measurement volume of only $0.3\,\text{cm}^3$. Theoretical analysis shows that fundamental sensitivity limits of this device are below $0.01\,\text{fT}\,\text{Hz}^{-1/2}$. We also demonstrate simple multichannel operation of the magnetometer, and localization of magnetic field sources with a resolution of 2 mm.

Ultrasensitive magnetometers have found a wide range of applications, from condensed-matter experiments[5] and gravitational wave detection[6], to detection of NMR signals[7,8], studies of palaeomagnetism[9], non-destructive testing[10], and underwater ordnance detection[11]. However, the most notable application of magnetic field sensors has been in the area of biomagnetism[12,13], that is, the detection of the weak magnetic fields produced by the human brain, heart and other organs. For example, measurements of the magnetic field produced by the brain are used to diagnose epilepsy, and to study neural responses to auditory and visual stimuli. Low-temperature superconducting quantum interference device (SQUID) sensors[14–16], which so far have dominated all of the above-mentioned applications, have reached sensitivity levels of 0.9–$1.4\,\text{fT}\,\text{Hz}^{-1/2}$ with a pick-up coil area of the order of $1\,\text{cm}^2$. In the low-frequency range of interest for biomagnetic studies (<100 Hz) their noise is typically somewhat higher, whereas commercial SQUID magnetometers typically[17] have noise of about $5\,\text{fT}\,\text{Hz}^{-1/2}$, partly due to magnetic noise generated by electrically conductive radiation-shielding of the liquid-helium dewars[18].

Atomic magnetometers rely on a measurement of the Larmor precession of spin-polarized atoms in a magnetic field[19]. The fundamental, shot-noise-limited sensitivity of an atomic magnetometer is given by

$$\delta B = \frac{1}{\gamma\sqrt{nT_2Vt}} \tag{1}$$

where n is the number density of atoms, γ is their gyromagnetic ratio, T_2 is the transverse spin relaxation time, V is the measurement volume, and t is the measurement time[20]. The value of γ in equation (1) depends on the details of the magnetometer operation. For a commonly used Zeeman transition with $\Delta m = 1$, $\gamma = g\mu_B/\hbar(2I + 1)$, where I is the nuclear spin of the alkali metal, μ_B is the Bohr magneton, and $g \approx 2$. In our magnetometer operating at zero field, the effective γ for sensitivity estimates is $\gamma = g\mu_B/\hbar$ (equation (7) of ref. 21).

Most atomic magnetometers use a polarized alkali-metal vapour (K, Rb, Cs), and their transverse spin relaxation time is limited by spin-exchange collisions between alkali atoms. In one implementation of such a magnetometer[3,22], the shot-noise sensitivity was estimated to be $0.3\,\text{fT}\,\text{Hz}^{-1/2}$ for a 500-cm^3 cell. In another state-of-the-art magnetometer[2], the actual sensitivity was estimated to be $1.8\,\text{fT}\,\text{Hz}^{-1/2}$ with a bandwidth of about 1 Hz and a measurement volume of 1,800 cm^3.

We recently demonstrated operation of a spin-exchange relaxation-free (SERF) magnetometer[21] where broadening due to spin-exchange collisions is completely eliminated by operating at a high alkali-metal density in a very low magnetic field. The remaining broadening is determined by spin-relaxation collisions, which transfer spin angular momentum to rotational momentum of